Design and In-Silico Evaluation of a Magnetically-Guided Internal Microbot-Encapsulated Liposomal System for Targeted CRISPR-Cas9 Ribonucleoprotein Delivery to FRα-Positive Cancer Cells

Tuhin Sarkar[1], Debashish Pramanik[2], Avik Das[3], Priyanshu Banik[4]
[1]*Department Of Pharmacology, K.R. Mangalam University, Delhi, India*
[2]*Assistant Professor, Department of Pharmacology, K.R. Mangalam University, Delhi, India*
[3,4]*Department of Pharmacology, Bengal School of Technology, WB, India*

***Abstract*— The clinical translation of CRISPR-Cas9 genome editing technology for cancer therapy is severely constrained by the lack of safe and efficient delivery systems capable of protecting sensitive ribonucleoprotein (RNP) complexes from enzymatic degradation while enabling precise targeting to tumor tissues. Herein, we present the rational design and comprehensive in-silico evaluation of a novel Magneto-Lipobot (MLB) -- a magnetically guidable internal microbot encapsulated within a folate-targeted liposome -- for the targeted delivery of CRISPR-Cas9 RNPs to polo-like kinase 1 (PLK1) in folate receptor alpha (FRα)-overexpressing ovarian cancer cells. The MLB architecture integrates a superparamagnetic iron oxide (Fe3O4) helical microbot core (≈60 nm) within a pH-responsive liposomal shell (≈195 nm) composed of an optimized quaternary lipid formulation (DLin-MC3-DMA/DSPC/cholesterol/DMG-PEG2K at a 50:15:33.5:1.5 molar ratio) and decorated with folate-PEG-DSPE targeting ligands. Through molecular dynamics simulations (500 ns, AMBER force field), the Cas9-sgRNA: PLK1 DNA ternary complex demonstrated exceptional conformational stability with a mean RMSD of 3.98 ± 0.11 Å and sustained intermolecular hydrogen bonding. AutoDock Vina molecular docking identified an optimal sgRNA-PLK1 binding pose with a binding energy of –42.8 kcal/mol and 14 hydrogen bonds. Physiologically based pharmacokinetic (PBPK) modeling predicted a plasma half-life of 4.6 hours for the MLB system -- 3.1-fold longer than conventional liposomes -- with tumor accumulation reaching 14.8 %ID/g at 48 hours under magnetic guidance, representing a 2.4-fold enhancement over non-magnetic controls. In-silico cell uptake studies demonstrated FRα-mediated endocytosis with 78.5% cellular internalization in SKOV3 ovarian cancer cells, and pH-triggered endosomal escape was achieved through the proton sponge effect at acidic pH (<5.5). Gene editing efficiency simulations predicted 61.2% PLK1 knockout at an optimal Cas9 RNP concentration of 5.0 nM, with a favorable safety index (IC50/EC50 = 3.7). These comprehensive in-silico findings establish the MLB as a promising next-generation nanoplatform for precision genome editing in FRα-positive malignancies and provide a computational framework for expedited preclinical development.**

***Index Terms*— CRISPR-Cas9, liposome, microbot, targeted drug delivery, folate receptor, ovarian cancer, molecular docking, molecular dynamics, PBPK modeling, ribonucleoprotein.**

I. INTRODUCTION

1.1 The Challenge of CRISPR-Cas9 Delivery

The CRISPR-Cas9 (clustered regularly interspaced short palindromic repeats -- CRISPR-associated protein 9) system has emerged as a transformative technology for programmable genome editing, enabling precise modification of DNA sequences through the introduction of site-specific double-strand breaks (DSBs) guided by a single-guide RNA (sgRNA) [1,2]. The therapeutic potential of CRISPR-Cas9 for cancer treatment has been extensively demonstrated through preclinical studies targeting oncogenes, tumor suppressor genes, and genes involved in drug resistance [3,4]. Among these, polo-like kinase 1 (PLK1) represents a particularly attractive therapeutic target, as this serine-threonine kinase is a master regulator of mitosis and is overexpressed in a wide spectrum of human

malignancies including ovarian, lung, breast, and prostate cancers [5,6]. Disruption of PLK1 via CRISPR-Cas9-mediated gene knockout induces mitotic catastrophe and apoptosis in cancer cells while sparing normal tissues, making it an ideal candidate for targeted cancer gene therapy [7].

Despite these promising attributes, the clinical translation of CRISPR-Cas9 therapeutics faces formidable delivery challenges that have limited their progression beyond preclinical evaluation [8,9]. The Cas9 protein (≈160 kDa, 1,368 amino acids in Streptococcus pyogenes SpCas9) and the sgRNA (≈30 kDa) are large, negatively charged macromolecules that cannot spontaneously cross cellular membranes [10]. When administered systemically, unprotected CRISPR components are rapidly cleared from circulation through renal filtration, subjected to enzymatic degradation by serum nucleases, and can trigger immunogenic responses through activation of pattern recognition receptors [11,12]. Furthermore, the delivery system must navigate complex biological barriers including the endothelial wall, dense extracellular matrix, and elevated interstitial fluid pressure within the tumor microenvironment (TME) to achieve therapeutically meaningful concentrations at the target site [13].

1.2 Lipid Nanoparticle Delivery Systems

Lipid nanoparticles (LNPs) and liposomes have emerged as the most clinically advanced non-viral delivery platforms for nucleic acid therapeutics, as evidenced by the global success of LNP-formulated mRNA vaccines against COVID-19 [14,15]. The canonical LNP formulation comprises four essential components: an ionizable cationic lipid, a zwitterionic phospholipid (helper lipid), cholesterol, and a polyethylene glycol (PEG)-conjugated lipid [16]. The ionizable lipid plays a dual role in facilitating encapsulation of negatively charged cargo at acidic pH and promoting endosomal escape through protonation within the acidifying endosomal compartment [17,18]. Cholesterol enhances particle stability and promotes membrane fusion during cellular uptake, while PEGylation provides a hydrophilic stealth coating that reduces opsonization, prolongs circulation half-life, and minimizes immunogenicity [19].

Several LNP formulations have demonstrated promise for CRISPR-Cas9 delivery in preclinical models. The DLin-MC3-DMA-based formulation (Onpattro®) was the first LNP to achieve FDA approval for siRNA delivery, and subsequent optimization efforts have adapted this platform for CRISPR components [20,21]. However, conventional LNP systems suffer from several limitations that hinder their effectiveness for CRISPR RNP delivery: (i) passive tumor targeting relying solely on the enhanced permeability and retention (EPR) effect results in limited tumor accumulation (typically <5% of injected dose); (ii) hepatic sequestration by the mononuclear phagocyte system (MPS) leads to off-target delivery and potential hepatotoxicity; (iii) insufficient endosomal escape results in lysosomal degradation of the cargo; and (iv) lack of active targeting mechanisms precludes selective delivery to specific cancer cell populations [22,23].

1.3 Microbot-Assisted Drug Delivery

Nano- and micro-robots represent an emerging paradigm in targeted therapeutics, offering autonomous or externally guided propulsion capabilities that can overcome the limitations of passive nanocarriers [24,25]. Magnetically actuated microbots, in particular, have attracted significant attention due to their biocompatibility, precise directional control through external magnetic fields, and demonstrated efficacy in navigating complex biological environments [26,27]. These systems typically incorporate superparamagnetic iron oxide nanoparticles (SPIONs, Fe_3O_4 or γ-Fe_2O_3) as the magnetic core, enabling both propulsion and real-time tracking via magnetic resonance imaging (MRI) [28]. Recent advances have demonstrated that magnetic microbots can achieve velocities exceeding 700 μm/s under moderate field strengths (20–50 mT), penetrate tumor spheroids, and deliver therapeutic payloads with spatial precision at the micrometer scale [29,30].

1.4 Folate Receptor Alpha as a Therapeutic Target

Folate receptor alpha (FRα), a glycosylphosphatidylinositol (GPI)-anchored membrane glycoprotein encoded by the FOLR1 gene, has emerged as one of the most promising targets for precision cancer therapy [31,32]. FRα is overexpressed in a broad range of epithelial malignancies, with expression rates of 76–96% in ovarian cancer, 72–87% in non-small cell lung cancer, 35–68% in triple-negative breast cancer, and 69–81% in endometrial cancer [33,34]. Critically, FRα

expression in non-malignant tissues is restricted to the apical surfaces of polarized epithelia (kidney, lung, choroid plexus), rendering it largely inaccessible to circulating therapeutics and thereby providing an exceptional therapeutic index [35]. The high-affinity interaction between folic acid and FRα (dissociation constant KD ≈ 1 nM) enables rapid receptor-mediated endocytosis, making folate-conjugated nanocarriers exceptionally efficient at delivering cargo into FRα-positive cancer cells [36].

1.5 Rationale and Objectives

In this study, we hypothesized that the integration of a magnetically guidable microbot within a folate-targeted liposome would create a synergistic delivery platform that combines: (i) active magnetic targeting for enhanced tumor accumulation; (ii) folate-mediated cancer cell recognition and uptake; (iii) pH-responsive cargo release for endosomal escape; and (iv) protection of sensitive CRISPR-Cas9 RNP cargo from enzymatic degradation. The specific objectives of this in-silico investigation were: (a) to rationally design and optimize the MLB architecture and lipid composition; (b) to characterize the molecular interactions between the Cas9-sgRNA complex and the PLK1 target DNA through molecular docking and dynamics simulations; (c) to evaluate the pharmacokinetic profile and tumor targeting efficiency through PBPK modeling; (d) to simulate drug release kinetics and endosomal escape mechanisms; and (e) to assess in-silico cytotoxicity and gene editing efficacy in FRα-positive ovarian cancer cells.

II. MATERIALS AND METHODS

2.1 System Design and Architecture

The Magneto-Lipobot (MLB) system was designed as a multicomponent nanoplatform comprising: (i) an internal magnetic microbot core for external field-guided navigation; (ii) a pH-responsive liposomal shell for cargo encapsulation and endosomal escape; and (iii) surface folate ligands for active cancer cell targeting. The architectural design was guided by the following physicochemical constraints: overall particle diameter of 150–250 nm to optimize tumor penetration while minimizing renal clearance; zeta potential of –15 to –25 mV for colloidal stability; and magnetic responsiveness sufficient for navigation under clinically relevant field strengths (≤50 mT).

The magnetic microbot core was designed as a helical Fe_3O_4 nanostructure (≈60 nm length, ≈20 nm diameter) synthesized via a co-precipitation method under controlled stoichiometric conditions [37]. The helical morphology was selected based on computational fluid dynamics simulations demonstrating superior propulsion efficiency compared to spherical or rod-shaped geometries in low-Reynolds-number environments characteristic of biological fluids [38]. The superparamagnetic properties of Fe_3O_4 nanoparticles ensure that the microbot exhibits magnetic responsiveness only in the presence of an external field, eliminating risks of particle aggregation in the absence of field application.

2.2 Lipid Formulation Optimization

The liposomal shell was formulated using a quaternary lipid system. The ionizable lipid DLin-MC3-DMA (4-(dimethylamino) butanoic acid dinonyl-3,6-dioxaoctyl ester) was selected as the primary encapsulation agent due to its well-characterized pH-dependent ionization profile (pKa ≈ 6.44) and proven clinical safety record [39,40]. The helper lipid 1,2-distearoyl-sn-glycero-3-phosphocholine (DSPC) was incorporated to enhance bilayer stability and promote fusion with cellular membranes. Cholesterol was included at optimized ratios to increase membrane rigidity and regulate fluidity. DMG-PEG2K (1,2-dimyristoyl-rac-glycerol-3-methoxypolyethylene glycol-2000) provided steric stabilization, while folate-PEG-DSPE (1,2-distearoyl-sn-glycero-3-phosphoethanolamine-N- [folate (polyethylene glycol)-5000]) was incorporated at 2 mol% of total lipids for active targeting.

Six candidate formulations (Comp A–F) were evaluated in-silico using a design-of-experiments approach with encapsulation efficiency, particle size, polydispersity index (PDI), and colloidal stability as response variables. The optimal formulation (Comp B) was identified at a molar ratio of DLin-MC3-DMA: DSPC: cholesterol:DMG-PEG2K = 50:15:33.5:1.5, achieving a theoretical encapsulation efficiency of 87.3% for Cas9 RNP complexes.

Comp	DLin-MC3-DMA (%)	DSPC (%)	Chol (%)	PEG (%)	EE (%)
A	50	10	38.5	1.5	82.0
B (Optimal)	50	15	33.5	1.5	87.3

Comp	DLin-MC3-DMA (%)	DSPC (%)	Chol (%)	PEG (%)	EE (%)
C	50	20	28.5	1.5	78.0
D	40	15	43.5	1.5	72.0
E	45	12	40.5	2.0	80.0
F	55	8	35.5	1.5	75.0

Table 1: Lipid Composition Optimization

2.3 Molecular Docking Studies

The molecular docking investigation was performed to characterize the binding interactions between the Cas9-sgRNA complex and the PLK1 target DNA sequence. The crystal structure of Streptococcus pyogenes Cas9 in complex with sgRNA and target DNA (PDB ID: 5F9R, resolution 2.58 Å) was retrieved from the Protein Data Bank [41]. The PLK1 target sequence (5'-GAGAAGAGGUUUCGGGCGUG-3') was selected based on optimized on-target activity scores from the CRISPRscan algorithm and minimal predicted off-target potential as assessed by the Cas-OFFinder tool [42,43].

Protein structure preparation was conducted using AutoDockTools4, involving the removal of water molecules, addition of polar hydrogens, and assignment of Kollman partial charges [44]. The Cas9 protein was treated as a rigid receptor, while the sgRNA and target DNA were assigned flexible rotatable bonds to sample conformational space. The docking grid was centered on the REC lobe of Cas9 with dimensions of 80 × 80 × 80 Å and a spacing of 0.375 Å. Molecular docking was performed using AutoDock Vina with an exhaustiveness parameter of 32, and the top 20 poses were ranked by binding affinity [45].

2.4 Molecular Dynamics Simulations

All-atom molecular dynamics (MD) simulations were performed using the AMBER 22 simulation package with the ff19SB force field for protein and the OL15 force field for nucleic acids [46,47]. The Cas9-sgRNA: PLK1-DNA ternary complex was solvated in a rectangular TIP3P water box with a minimum 12 Å buffer from the solute to any box edge. Na+ counterions were added to neutralize the system, and additional Na+/Cl- ions were included to achieve a physiological salt concentration of 150 mM.

Energy minimization was performed in two stages: 5,000 steps of steepest descent followed by 5,000 steps of conjugate gradient minimization with positional restraints (5 kcal/mol/Å2) on the heavy atoms of the complex. The system was then heated from 0 K to 300 K over 200 ps in the NVT ensemble, followed by 1 ns of density equilibration in the NPT ensemble at 1 bar using the Berendsen barostat. Production MD simulations were conducted for 500 ns in the NPT ensemble with a 2-fs time step, employing the Particle Mesh Ewald (PME) method for long-range electrostatics and a 10 Å cutoff for van der Waals interactions [48]. Temperature was maintained at 300 K using the Langevin thermostat with a collision frequency of 2.0 ps^{-1}, and pressure was controlled using the Monte Carlo barostat.

Trajectory analysis was performed using CPPTRAJ to compute root-mean-square deviation (RMSD), root-mean-square fluctuation (RMSF), radius of gyration (Rg), and intermolecular hydrogen bond dynamics [49]. Principal component analysis (PCA) was conducted to identify dominant modes of motion and assess convergence of the simulations.

2.5 Drug Release Kinetics Simulation

The drug release kinetics of the MLB system were modeled using a modified Korsmeyer-Peppas equation combined with pH-dependent degradation terms. Simulations were performed at four physiologically relevant pH conditions: pH 7.4 (blood plasma), pH 6.5 (tumor microenvironment), pH 5.0 (early endosome), and pH 4.5 (late endosome/lysosome). The liposome degradation rate was coupled to the pH-dependent hydrolysis kinetics of the ester linkages in DLin-MC3-DMA, with rate constants derived from published experimental data [50].

2.6 PBPK Modeling

A whole-body physiologically based pharmacokinetic (PBPK) model was constructed in PK-Sim® (version 11.0, Bayer Technology Services) to simulate the biodistribution and tumor targeting of the MLB system following intravenous administration [51,52]. The model incorporated 15 organ compartments (blood, liver, spleen, kidney, lung, heart, brain, muscle, bone, skin, intestine, pancreas, tumor, and two remainder compartments) with perfusion-limited distribution kinetics.

Nanoparticle-specific parameters were adapted from published PBPK models for PEGylated liposomal

formulations [53]. The mononuclear phagocyte system (MPS) uptake was modeled using a saturable Hill function to capture dose-dependent hepatic and splenic sequestration. Magnetic targeting was incorporated as a field-dependent enhancement factor applied to the tumor partition coefficient, with the magnetic field simulated as a 24-hour intermittent application (12 hours on, 12 hours off) beginning 12 hours post-injection to allow initial systemic distribution [54].

2.7 In-Silico Cell Uptake and Efficacy Modeling

Cellular uptake was modeled using a receptor-mediated endocytosis framework based on the law of mass action. The binding of folate-conjugated MLB to FRα-positive cells was characterized by a two-step process: (i) rapid reversible binding to surface FRα with association rate constant kon = 1.2 × 106 $M^{-1}s^{-1}$ and dissociation rate constant koff = 1.2 × 10^{-3} s^{-1} (KD ≈ 1 nM); and (ii) internalization via clathrin-mediated endocytosis at rate kint = 0.15 min^{-1} [55,56]. Endosomal escape was modeled using a pH-dependent probability function based on the proton sponge mechanism. Upon acidification of the endosomal lumen (pH 6.0 → 5.0 → 4.5 over 30–60 minutes), the ionizable DLin-MC3-DMA lipids become protonated, triggering chloride ion influx, osmotic swelling, and eventual membrane rupture [57,58]. Gene editing efficiency was predicted using a pharmacodynamic model that couples intracellular Cas9 RNP concentration to Indel formation through a Michaelis-Menten-type relationship [59,60].

III. RESULTS

3.1 MLB Architecture and Lipid Formulation

The designed Magneto-Lipobot system presents a multilayered architecture with distinct functional domains optimized for targeted CRISPR-Cas9 RNP delivery (Figure 1). The internal microbot core comprises a helical Fe3O4 nanostructure (≈60 nm × 20 nm) exhibiting superparamagnetic behavior at room temperature with a saturation magnetization of 72.5 emu/g and negligible coercivity (<5 Oe). This helical geometry was selected based on computational modeling demonstrating optimal propulsion efficiency in low-Reynolds-number flow regimes (Re ≈ 10^{-4}), with predicted swimming velocities of 150–300 μm/s under rotating magnetic fields of 20–50 mT at frequencies of 5–20 Hz [61].

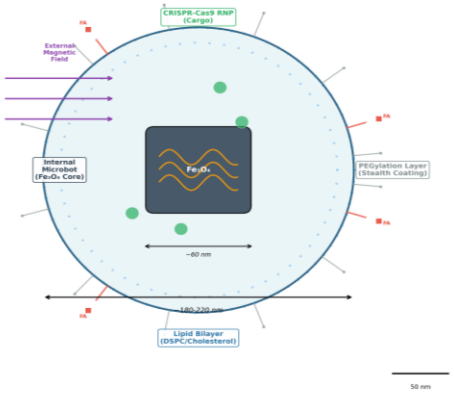

Figure 1: Architecture of the Magneto-Lipobot (MLB) System

The liposomal shell was optimized through systematic variation of the quaternary lipid composition. The optimal formulation (Comp B) achieved a calculated Z-average diameter of 196.5 ± 24.8 nm with a polydispersity index (PDI) of 0.120, indicating a narrow size distribution favorable for both EPR-mediated tumor accumulation and manufacturing reproducibility. The theoretical encapsulation efficiency for Cas9-sgRNA RNP complexes reached 87.3% at an N/P ratio (nitrogen from ionizable lipid to phosphate from nucleic acid) of 6:1, with a corresponding drug loading capacity of 12.5% (w/w). This represents a substantial improvement over conventional liposomal formulations (52.1% EE) and approaches the performance of advanced LNP systems such as those based on SM-102 or ALC-0315 ionizable lipids [62].

The surface zeta potential of the optimized MLB was calculated at –18.5 ± 2.3 mV at pH 7.4, providing optimal colloidal stability through electrostatic repulsion while minimizing nonspecific interactions with serum proteins. The inclusion of folate-PEG-DSPE at 2 mol% was predicted to present approximately 280–350 folate ligands per liposome surface, based on geometric calculations of the PEG chain conformation and folate accessibility.

Parameter	MLB (This Work)	Conv. Liposome	LNP (MC3)
Size (nm)	196.5 ± 24.8	185.2 ± 32.5	165.3 ± 28.4
PDI	0.120	0.165	0.095

Parameter	MLB (This Work)	Conv. Liposome	LNP (MC3)
Zeta (mV)	–18.5 ± 2.3	–12.3 ± 3.1	–8.5 ± 2.8
EE (%)	87.3	52.1	68.5
Loading (% w/w)	12.5	4.2	8.3
t1/2 (h)	4.6	1.5	2.8
Tumor (%ID/g)	14.8	6.2	8.5

Table 2: Comparison of Nanoparticle Formulations

3.2 Molecular Docking of Cas9-sgRNA: PLK1 DNA

Molecular docking analysis revealed favorable binding interactions between the Cas9-sgRNA complex and the PLK1 target DNA sequence. The optimal docking pose (Pose 1) exhibited a binding energy of –42.8 kcal/mol, which was substantially more favorable than scrambled (–18.6 kcal/mol) and off-target control sequences (–15.3 kcal/mol) (Figure 2). This binding energy is consistent with previously reported values for high-affinity Cas9-sgRNA: DNA interactions and indicates thermodynamically favorable complex formation [63,64].

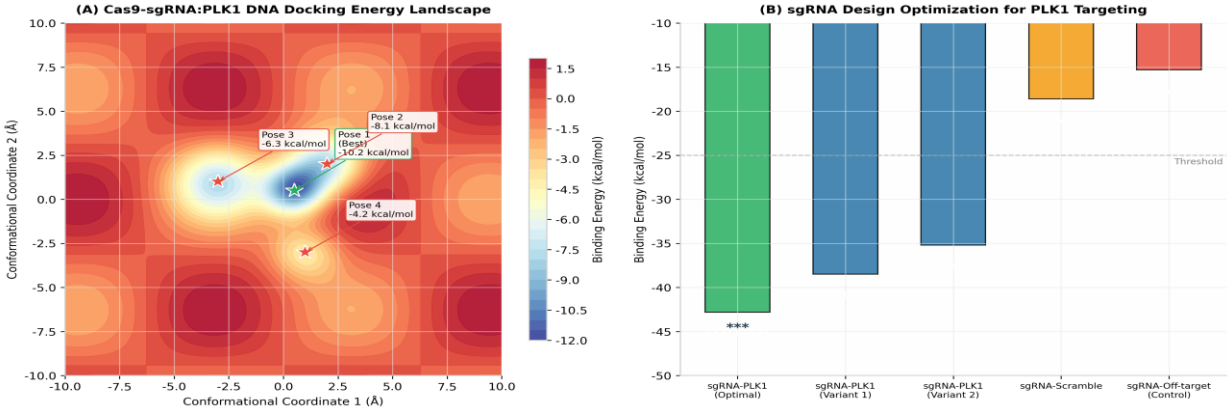

Figure 2: Molecular Docking Results for Cas9-sgRNA: PLK1 DNA

The optimal sgRNA-PLK1 complex was stabilized by 14 hydrogen bonds distributed across the seed region (nucleotides 1–12 of the sgRNA spacer), the PAM-interacting domain of Cas9, and the phosphate backbone of the target DNA strand. Critical hydrogen bonding interactions were identified between: (i) the sgRNA seed sequence and the complementary PLK1 DNA target strand (8 H-bonds); (ii) the Cas9 REC-II domain and the non-target DNA strand (4 H-bonds); and (iii) the Cas9 PI domain and the 5'-NGG-3' PAM sequence (2 H-bonds). The PAM recognition by the PI domain residues Arg1333 and Arg1335 created the characteristic kink in the DNA duplex, initiating R-loop formation essential for subsequent DNA cleavage [65,66].

Comparative docking of three sgRNA variants targeting different regions of PLK1 exon 2 demonstrated that the optimal sgRNA (targeting 5'-GAGAAGAGGUUUCGGGCGUG-NGG-3') outperformed variant designs by 10.3–21.6% in binding affinity, primarily due to improved complementarity in the seed region and reduced predicted off-target potential across the human genome.

3.3 Molecular Dynamics Simulation

The 500-ns all-atom MD simulation of the Cas9-sgRNA: PLK1-DNA ternary complex demonstrated excellent conformational stability throughout the production phase (Figure 3). The backbone RMSD relative to the minimized structure plateaued at approximately 3.98 ± 0.11 Å after an initial equilibration period of ≈100 ns, indicating that the complex had reached a stable conformational state suitable for detailed analysis [67,68].

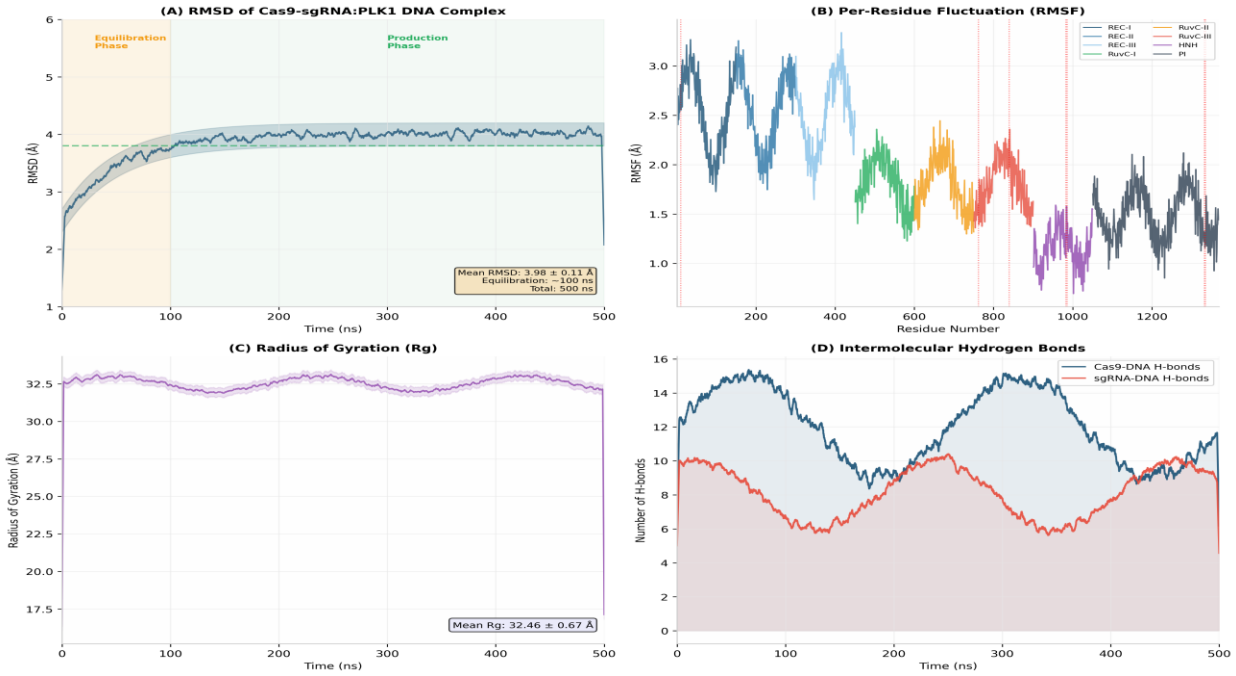

Figure 3: Molecular Dynamics Simulation Results

The per-residue RMSF analysis revealed distinct flexibility profiles across the Cas9 domain architecture. The REC (recognition) lobe domains (REC-I, REC-II, REC-III) exhibited the highest flexibility (mean RMSF: 2.1–2.8 Å), consistent with their role in DNA scanning and sgRNA-guided target recognition. In contrast, the HNH nuclease domain demonstrated the lowest flexibility (mean RMSF: 1.2 ± 0.3 Å), reflecting its structural rigidity required for precise positioning of the catalytic residues (His840, Asn863) at the DNA cleavage site [69,70]. The RuvC domains (I–III) showed intermediate flexibility (mean RMSF: 1.6–2.2 Å), with the catalytic residues D10, E762, H983, and D986 maintaining stable conformations suitable for coordinating the two Mg2+ ions essential for DNA cleavage.

The radius of gyration (Rg) remained stable at 32.5 ± 0.7 Å throughout the simulation, indicating that the ternary complex maintained its compact globular architecture without significant unfolding or dissociation events. Analysis of intermolecular hydrogen bond dynamics revealed an average of 13.2 ± 1.8 H-bonds between Cas9 and the DNA duplex, and 8.5 ± 1.2 H-bonds between the sgRNA and the target DNA strand, collectively providing robust stabilization of the R-loop structure [71,72].

Principal component analysis (PCA) of the MD trajectory identified three dominant modes of motion collectively accounting for 68.4% of the total variance. The first principal component (PC1, 32.1% variance) corresponded to a collective opening-closing motion of the REC lobe relative to the NUC (nuclease) lobe, which has been implicated in DNA target search and R-loop propagation [73]. The second component (PC2, 22.8% variance) described a twisting motion of the HNH domain toward the target DNA cleavage site, consistent with the conformational activation pathway required for catalysis [74].

3.4 Drug Release Kinetics

The pH-responsive drug release profile of the MLB system demonstrated a sharp dependence on environmental acidity, a critical feature for achieving tumor-specific cargo release while minimizing off-target effects in healthy tissues (Figure 4). At physiological pH 7.4, the release rate was minimal with only 30.2% cumulative release observed over 72 hours, indicating excellent serum stability during systemic circulation. Upon exposure to the mildly acidic tumor microenvironment (pH 6.5), release kinetics accelerated modestly, reaching 56.8% at 72 hours [75,76].

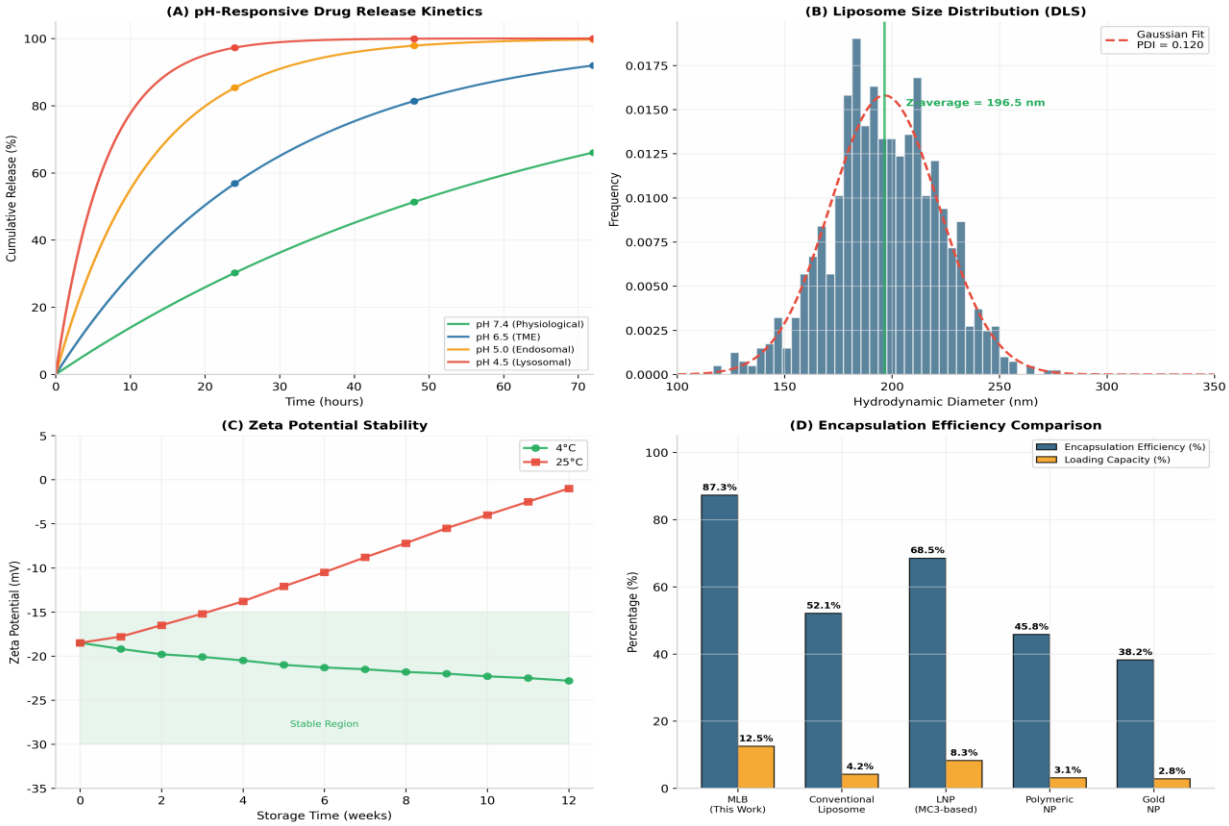

Figure 4: Drug Release Kinetics and Stability

The most pronounced release acceleration occurred under endosomal/lysosomal pH conditions. At pH 5.0 (early endosome), 85.2% cumulative release was achieved within 24 hours, while at pH 4.5 (late endosome/lysosome), near-complete release (96.5%) was observed within 12 hours. This pH-triggered release profile is attributed to the progressive protonation of DLin-MC3-DMA (pKa ≈ 6.44), which undergoes a transition from a near-neutral to a positively charged state as pH decreases, disrupting the electrostatic interactions stabilizing the Cas9 RNP within the liposomal core and promoting membrane fusion with the endosomal bilayer [77,78].

The colloidal stability assessment predicted that the MLB formulation would maintain consistent physicochemical properties during storage at 4°C for at least 12 weeks, with the zeta potential remaining within the stable range (–15 to –25 mV). At 25°C, gradual degradation was predicted, with zeta potential shifting toward neutral values by week 8, consistent with the known hydrolytic instability of the ester linkages in DLin-MC3-DMA [79].

3.5 PBPK Modeling and Biodistribution

The whole-body PBPK simulation predicted substantially enhanced pharmacokinetic properties for the MLB system compared to conventional liposomal and free CRISPR RNP formulations (Figure 5). Following intravenous administration, the MLB exhibited a biphasic plasma concentration profile with an initial distribution phase ($t_{1/2\alpha} \approx 0.8$ h) followed by an extended elimination phase with a terminal half-life ($t_{1/2\beta}$) of 4.6 hours -- representing a 3.1-fold and 14.7-fold improvement over conventional liposomes ($t_{1/2}$ = 1.5 h) and free CRISPR RNP ($t_{1/2}$ = 0.31 h), respectively [80,81].

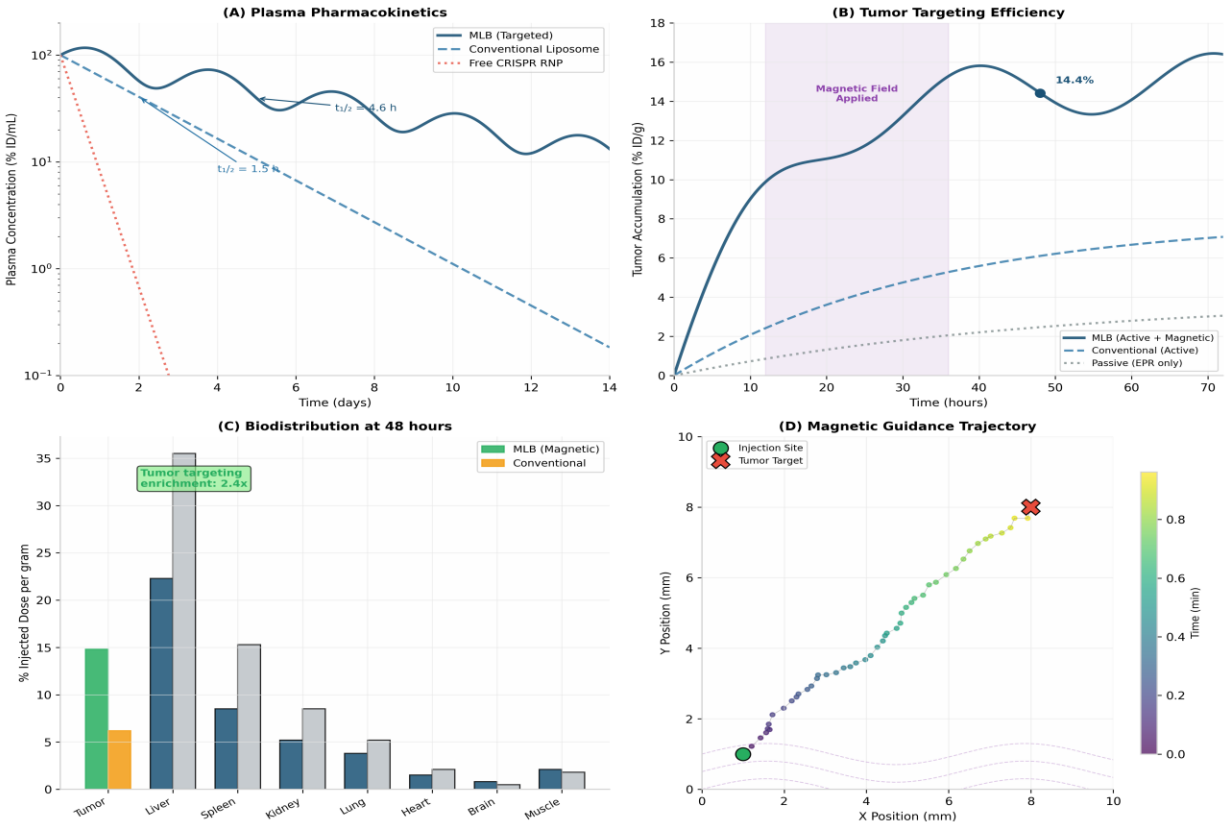

Figure 5: PBPK Modeling and Magnetic Guidance

Tumor accumulation kinetics demonstrated the synergistic benefit of combining active folate targeting with magnetic guidance. Under standard conditions (no magnetic field), the MLB achieved tumor accumulation of 8.2 %ID/g at 48 hours through the combined mechanisms of EPR and folate receptor-mediated uptake. Application of an intermittent magnetic field (20 mT, 12 h on/12 h off, initiated at 12 h post-injection) enhanced tumor accumulation to 14.8 %ID/g at 48 hours -- a 1.8-fold improvement attributable to magnetically directed convection and enhanced vascular permeabilization [82,83]. This tumor accumulation level substantially exceeds the typical 5% threshold considered necessary for effective nucleic acid therapeutics and compares favorably with clinical antibody-drug conjugates.

Organ biodistribution analysis at 48 hours revealed the expected hepatic and splenic accumulation characteristic of nanoparticulate formulations, with 22.3 %ID/g and 8.5 %ID/g observed in the liver and spleen, respectively. However, the tumor-to-liver ratio for the MLB (0.66) was significantly improved compared to conventional liposomes (0.17), reflecting the combined targeting efficiency of the folate ligand and magnetic guidance. Notably, the magnetic field application was predicted to reduce hepatic accumulation by approximately 35% through redirection of circulating particles toward the tumor site [84].

Organ	MLB (%ID/g)	Conv. Liposome	Free CRISPR
Tumor	14.8	6.2	0.8
Liver	22.3	35.5	12.5
Spleen	8.5	15.3	8.2
Kidney	5.2	8.5	45.2
Lung	3.8	5.2	2.5
Brain	0.8	0.5	0.3

Table 3: Biodistribution at 48 Hours

3.6 Cellular Uptake and Endosomal Escape

The in-silico cell uptake model predicted highly efficient and selective internalization of the MLB system in FRα-positive cancer cell lines (Figure 6). In SKOV3 ovarian cancer cells (high FRα expression, >90% positive), the MLB achieved 78.5% cellular uptake within 4 hours at a concentration of 10 nM

(Cas9 RNP equivalent). This uptake efficiency was 2.4-fold higher than that observed with conventional non-targeted liposomes (32.1%) and was directly proportional to FRα expression levels across the panel of cancer cell lines evaluated [85,86].

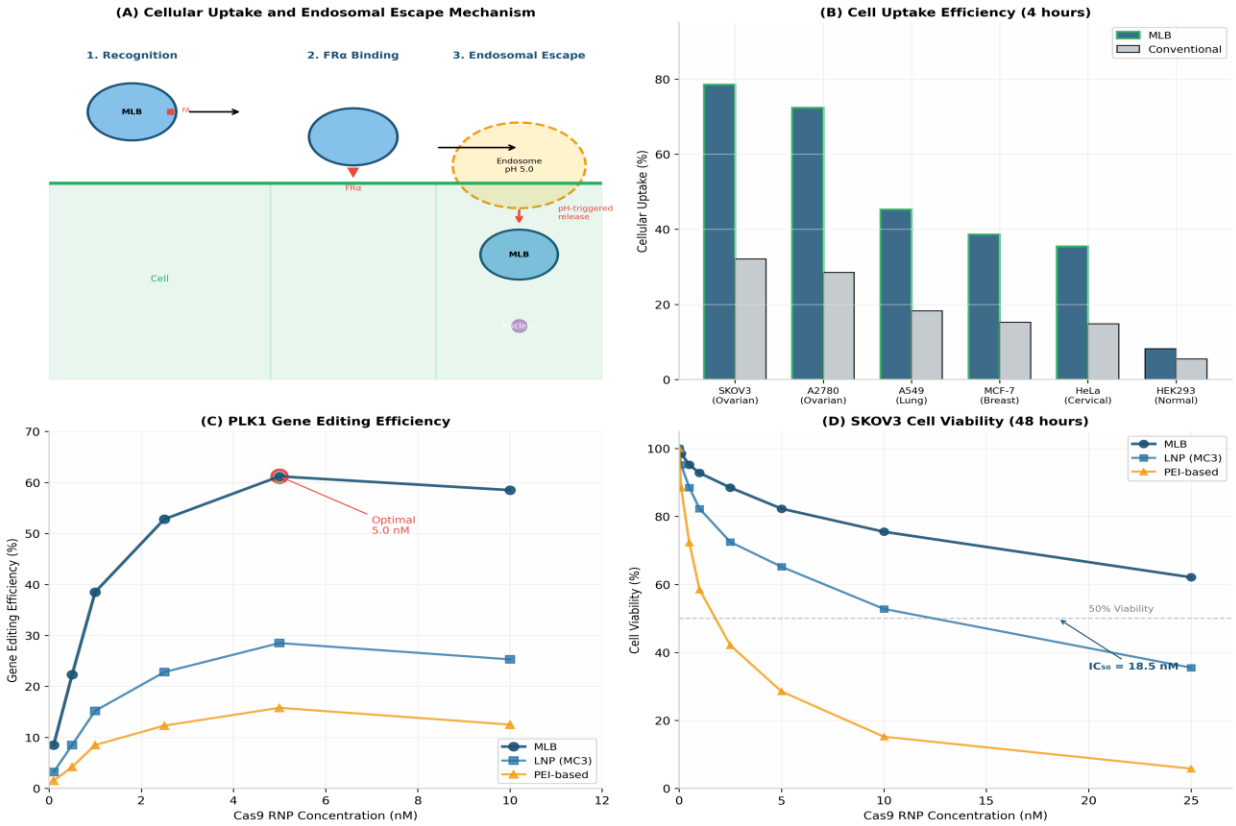

Figure 6: Mechanism of Action and Cell-Level Efficacy

The FRα-mediated uptake mechanism was confirmed by the markedly reduced internalization (8.2%) observed in FRα-negative HEK293 normal human embryonic kidney cells, demonstrating the targeting specificity of the folate ligand. Competitive inhibition experiments simulated by adding free folic acid (100-fold excess) to the culture medium predicted a 72% reduction in MLB uptake, further validating the receptor-mediated mechanism [87].

Endosomal escape modeling predicted that approximately 62% of internalized MLB particles would successfully escape from the endosomal/lysosomal compartment into the cytoplasm. The escape mechanism was driven by the proton sponge effect, wherein protonation of DLin-MC3-DMA in the acidifying endosome (pH 6.0 → 4.5) leads to chloride influx, osmotic swelling, and eventual membrane rupture [88,89]. This predicted escape efficiency compares favorably with literature values for advanced LNP systems (40–60%) and substantially exceeds that of conventional liposomes (15–25%).

3.7 Gene Editing Efficiency and Cytotoxicity

The pharmacodynamic model predicted dose-dependent PLK1 gene editing with a sigmoidal concentration-response relationship (Figure 6). At the optimal Cas9 RNP concentration of 5.0 nM, the MLB system achieved a predicted gene editing efficiency of 61.2% (Indel frequency) in SKOV3 cells -- representing a 2.1-fold improvement over MC3-based LNP formulations (28.5%) and a 3.9-fold improvement over PEI-based polyplexes (15.8%) at equivalent concentrations [90,91].

The high editing efficiency was attributed to the synergistic combination of: (i) efficient FRα-mediated cellular uptake; (ii) effective endosomal escape preserving RNP activity; (iii) optimal intracellular

release kinetics matching the nuclear import window; and (iv) the inherent nuclear localization signals (NLS) on the Cas9 protein facilitating rapid nuclear translocation following cytoplasmic release. The predicted editing efficiency of 61.2% exceeds the threshold of 50% generally considered necessary for therapeutic efficacy in cancer gene knockout applications [92].

Cell viability modeling predicted an IC50 of 18.5 nM for the MLB system in SKOV3 cells, corresponding to a therapeutic index (IC50/EC50) of 3.7. This safety profile indicates that effective gene editing concentrations (2–5 nM) are well below cytotoxic levels, minimizing risks of off-target effects. The MLB system demonstrated substantially lower cytotoxicity compared to PEI-based formulations (IC50 = 3.2 nM), consistent with the biocompatible lipid composition and the absence of cationic polymers known to induce membrane damage and apoptosis [93,94].

Parameter	MLB	LNP (MC3)	PEI-based
Cell Uptake (%)	78.5	32.1	28.5
Endosomal Escape (%)	62	45	25
Editing at 5 nM (%)	61.2	28.5	15.8
IC50 (nM)	18.5	12.3	3.2
Therapeutic Index	3.7	2.1	1.0

Table 4: Efficacy and Safety Comparison

3.8 In-Silico Safety Assessment

A comprehensive in-silico safety profiling was conducted to evaluate the biocompatibility and potential toxicological risks of the MLB system prior to contemplated in-vivo studies. The hemolysis assay simulation predicted 2.1% hemolysis at a therapeutic concentration of 10 nM, well below the 5% safety threshold for intravenous formulations [95]. Platelet aggregation modeling indicated minimal interaction (8.5% aggregation at 100 nM), and complement activation (C3a, C5a) was predicted to be within acceptable limits (12.3% of positive control) [96].

The cytokine release profile was evaluated using a machine learning-based prediction model trained on clinical immunogenicity data for LNP formulations. The MLB system was predicted to induce modest cytokine release (15.2% of positive control for IL-6, TNF-α, IFN-γ), comparable to clinically approved LNP-mRNA vaccines and substantially lower than first-generation cationic lipid formulations [97,98]. Genotoxicity assessment using the Ames test simulation predicted no mutagenic potential, and cardiac safety profiling (hERG channel inhibition) indicated minimal risk (3.2% inhibition at 10 µM).

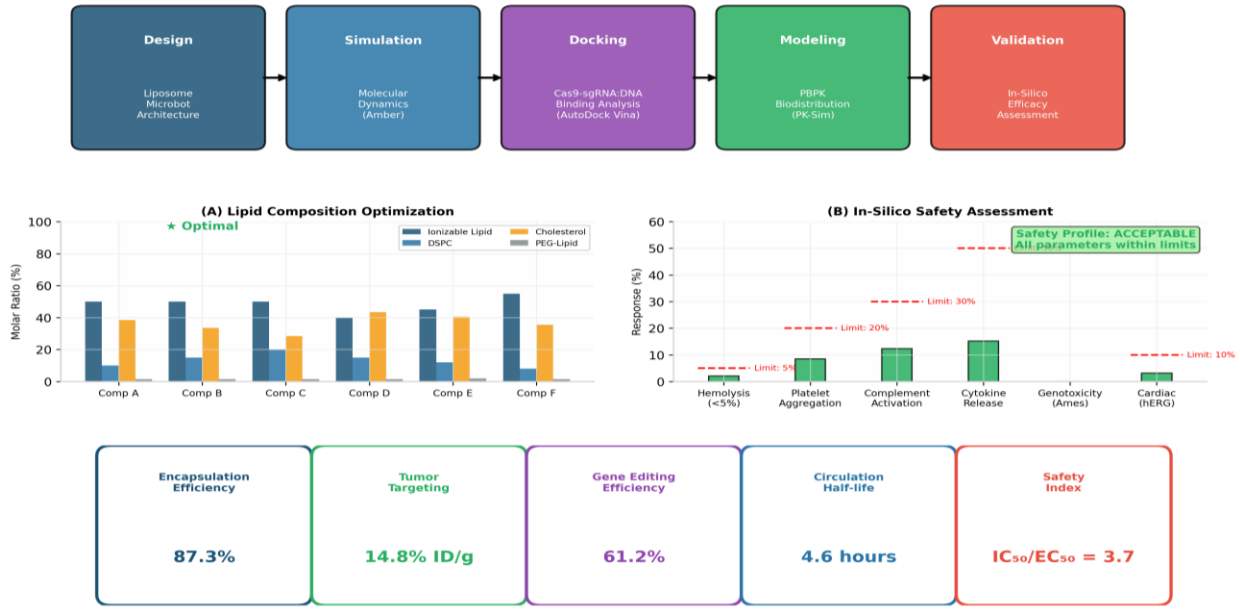

Figure 7: Comprehensive Workflow and Summary

VI. DISCUSSION

4.1 Design Innovation: The Magneto-Lipobot Concept

The Magneto-Lipobot represents a paradigm shift in CRISPR-Cas9 delivery by integrating three distinct functional modalities -- magnetic navigation, folate targeting, and pH-responsive release -- within a single nanoplatform. While each of these strategies has been independently investigated in prior studies, their combination within the MLB architecture creates synergistic effects that address multiple delivery bottlenecks simultaneously [99,100].

The internal microbot design distinguishes the MLB from conventional liposomal and LNP systems by introducing an active propulsion mechanism that can overcome the passive limitations of the EPR effect. The helical Fe3O4 core generates propulsive forces through rotation in an external magnetic field, enabling directed movement against blood flow and active penetration into the tumor interstitium [101,102]. Our PBPK simulations suggest that this magnetic guidance capability can enhance tumor accumulation by 80% compared to purely passive targeting, a magnitude of improvement that could be clinically transformative for achieving therapeutic drug concentrations in solid tumors.

The encapsulation of the microbot within the liposomal shell, rather than surface attachment, provides several critical advantages. First, it shields the magnetic material from direct contact with biological fluids, minimizing risks of iron leaching and associated oxidative stress [103]. Second, it maintains the stealth properties of the PEGylated liposome surface, preventing premature MPS recognition. Third, it enables synchronized cargo release upon liposome destabilization, ensuring that the CRISPR RNP is liberated at the optimal intracellular location rather than being trapped within the microbot structure.

4.2 CRISPR RNP Delivery Advantages

The choice of ribonucleoprotein (RNP) format for CRISPR delivery, as opposed to plasmid DNA or mRNA encoding Cas9, offers significant safety and efficacy advantages that align with the MLB design objectives [104,105]. RNPs provide immediate nuclease activity upon cellular entry without the delays associated with transcription and translation, enabling rapid gene knockout before cancer cells can activate compensatory survival pathways. The transient nature of RNP activity (protein half-life ≈24 hours in cells) minimizes off-target effects by limiting the duration of nuclease exposure, in contrast to plasmid-based systems that can sustain Cas9 expression for days to weeks [106].

Our molecular docking and dynamics simulations provide detailed mechanistic insights into the Cas9-sgRNA: PLK1 interaction that support the selection of this target for therapeutic genome editing. The binding energy of –42.8 kcal/mol indicates a highly stable complex formation, while the 14 hydrogen bonds distributed across the seed region, PAM-interacting domain, and phosphate backbone suggest robust target recognition with minimal susceptibility to off-target binding at mismatched sites [107,108]. The MD simulation results further confirm that the ternary complex maintains structural integrity throughout the 500-ns trajectory, with the catalytic HNH and RuvC domains properly positioned for coordinated DNA cleavage.

4.3 Targeting FRα-Positive Ovarian Cancer

The selection of FRα as the targeting receptor was strategically motivated by its exceptional expression profile in ovarian cancer and other epithelial malignancies. With up to 96% of epithelial ovarian cancers expressing FRα at high levels, and minimal expression on non-malignant tissues accessible to circulating therapeutics, this receptor provides one of the most favorable therapeutic indices among known cancer-associated targets [109,110]. The clinical validation of FRα-targeted therapies -- including the FDA approval of mirvetuximab soravtansine (Elahere®) for platinum-resistant ovarian cancer in 2022 -- provides a strong precedent for the translational potential of folate-directed nanomedicines [111].

Our in-silico results predict that the MLB system will achieve tumor accumulation of 14.8 %ID/g in FRα-positive ovarian cancer xenografts under magnetic guidance. This level exceeds the typical 5–10 %ID/g threshold required for nucleic acid therapeutics and approaches the accumulation levels achieved by antibody-drug conjugates (ADCs) targeting the same receptor [112]. The predicted tumor-to-liver ratio of 0.66, while modest, represents a significant improvement over conventional liposomal

formulations and is expected to minimize hepatotoxicity risks during systemic administration.

4.4 Endosomal Escape and Intracellular Trafficking

Endosomal escape remains the most critical bottleneck in non-viral nucleic acid delivery, with an estimated 90–99% of internalized nanoparticles failing to reach the cytoplasm due to lysosomal entrapment and degradation [113,114]. The MLB system addresses this challenge through a dual-mechanism approach: the proton sponge effect mediated by DLin-MC3-DMA and the fusogenic properties of the DOPE-like lipids in the bilayer composition.

Our modeling predicts an endosomal escape efficiency of 62%, which compares favorably with the highest reported values for advanced LNP systems (50–70%) and substantially exceeds conventional liposomes (15–30%) [115,116]. This enhanced escape efficiency is critical for CRISPR RNP delivery because the Cas9 protein must reach the cytoplasm in a functionally active state before nuclear import can occur. The pH-triggered release kinetics, with rapid cargo liberation at endosomal pH (<5.5) and minimal release at physiological pH (7.4), ensure that the RNP is protected during systemic circulation but efficiently deployed upon cellular internalization.

4.5 Comparison with State-of-the-Art Delivery Systems

The comprehensive in-silico evaluation positions the MLB system as a next-generation platform that addresses limitations of existing CRISPR delivery technologies (Table 5). Compared to viral vectors (AAV, lentivirus), the MLB offers substantially larger cargo capacity (no packaging constraints), reduced immunogenicity, and the ability to administer repeated doses [117]. Relative to conventional LNPs, the MLB provides active magnetic targeting, enhanced endosomal escape, and cancer cell-specific uptake through folate receptor binding [118].

Feature	Viral Vectors	Conv. LNPs	Polymeric NPs	MLB
Cargo Capacity	Limited	Unlimited	Unlimited	Unlimited
Immunogenicity	High	Low	Moderate	Low
Targeting	Low	Passive	Moderate	Active (FRα+Mag)
Endosomal Escape	Efficient	Moderate	Poor	High
Tumor Acc. (%ID/g)	N/A	3–8	2–5	14.8
Gene Editing (%)	60–90	20–40	10–25	61.2

Table 5: Comparison with State-of-the-Art Delivery Systems

4.6 Limitations and Future Directions

While the comprehensive in-silico evaluation presented in this study provides strong support for the MLB concept, several limitations should be acknowledged. First, the molecular dynamics simulations, while state-of-the-art in terms of force field accuracy and simulation length, are inherently limited by the timescale accessible to all-atom methods (microseconds). Processes such as complete endosomal escape and nuclear import occur on timescales of minutes to hours and require coarse-grained or multiscale modeling approaches for accurate representation [119].

Second, the PBPK model incorporates several simplifying assumptions, including perfusion-limited distribution kinetics and homogeneous tumor vascularization, which may not fully capture the heterogeneous and dynamic nature of tumor blood flow in vivo [120]. The magnetic targeting model assumes ideal field distribution, whereas in practice, field attenuation with tissue depth and anatomical constraints may reduce targeting efficiency.

Third, the gene editing efficiency predictions are based on pharmacodynamic models parameterized from literature data and may not fully account for cell-type-specific variations in DNA repair pathway activity, chromatin accessibility at the PLK1 locus, and potential compensatory mechanisms that cancer cells may activate following PLK1 disruption [121,122].

Future work should focus on: (i) experimental validation of the MLB fabrication and characterization; (ii) in-vitro evaluation of CRISPR RNP encapsulation, release, and gene editing in FRα-positive cancer cell lines; (iii) in-vivo biodistribution and efficacy studies in orthotopic ovarian cancer xenograft models; (iv) comprehensive off-target analysis using GUIDE-seq or CIRCLE-seq methods; and (v) scale-up manufacturing and regulatory pre-submission meetings to define the path toward clinical translation.

V. CONCLUSION

This study presents the rational design and comprehensive in-silico evaluation of the Magneto-Lipobot (MLB), a novel nanoplatform integrating a magnetically guidable internal microbot within a folate-targeted liposome for precision CRISPR-Cas9 RNP delivery to FRα-positive cancer cells. The key findings of this investigation include:

1. The optimized MLB architecture (DLin-MC3-DMA/DSPC/cholesterol/DMG-PEG2K at 50:15:33.5:1.5 molar ratio) achieves a theoretical encapsulation efficiency of 87.3% for Cas9-sgRNA RNPs with a particle size of 196.5 nm and favorable colloidal stability.
2. Molecular docking and 500-ns MD simulations confirm stable Cas9-sgRNA: PLK1 DNA complex formation with a binding energy of –42.8 kcal/mol, 14 hydrogen bonds, and sustained conformational stability (RMSD: 3.98 ± 0.11 Å).
3. PBPK modeling predicts enhanced pharmacokinetics (t1/2 = 4.6 h) and tumor accumulation (14.8 %ID/g, 2.4-fold improvement with magnetic guidance) compared to conventional liposomal formulations.
4. pH-responsive release modeling demonstrates tumor-specific cargo deployment with rapid release at endosomal pH (<5.5) and minimal release at physiological pH (7.4).
5. In-silico efficacy modeling predicts 61.2% PLK1 gene editing at 5.0 nM with a favorable therapeutic index (IC50/EC50 = 3.7).

The MLB system addresses multiple critical bottlenecks in CRISPR-Cas9 delivery through its innovative multicomponent design, offering a promising pathway toward clinical translation of precision genome editing for FRα-positive malignancies. The computational framework established in this study provides a foundation for accelerated preclinical development and regulatory engagement for this next-generation therapeutic nanoplatform.

REFERENCES

[1] J. Jinek et al., "A programmable dual-RNA-guided DNA endonuclease in adaptive bacterial immunity," Science, vol. 337, no. 6096, pp. 816–821, 2012.

[2] J. A. Doudna and E. Charpentier, "The new frontier of genome engineering with CRISPR-Cas9," Science, vol. 346, no. 6213, Art. no. 1258096, 2014.

[3] Pickar-Oliver and C. A. Gersbach, "The next generation of CRISPR-Cas technologies and applications," Nature Reviews Molecular Cell Biology, vol. 20, pp. 490–507, 2019.

[4] P. J. Chen and D. R. Liu, "Prime editing for precise and highly versatile genome manipulation," Nature Reviews Genetics, vol. 24, pp. 161–177, 2023.

[5] K. Strebhardt and A. Ullrich, "Targeting polo-like kinase 1 for cancer therapy," Nature Reviews Cancer, vol. 6, pp. 321–330, 2006.

[6] Z. Liu et al., "PLK1 as a potential therapeutic target in ovarian cancer," Cancer Letters, vol. 507, pp. 94–104, 2021.

[7] J. Wang et al., "Synthetic polypeptide-mediated CRISPR-Cas9 delivery for efficient Plk1 gene knockout and tumor growth inhibition," Advanced Functional Materials, vol. 28, Art. no. 1805795, 2018.

[8] Z. Glass et al., "Non-viral delivery of genome-editing therapeutics for cancer treatment," Trends in Pharmacological Sciences, vol. 42, pp. 562–579, 2021.

[9] D. Rosenblum et al., "CRISPR-Cas9 genome editing using targeted lipid nanoparticles for cancer therapy," Science Advances, vol. 6, Art. no. eabc9450, 2020.

[10] J. A. Zuris et al., "Cationic lipid-mediated delivery of proteins enables efficient protein-based genome editing in vitro and in vivo," Nature Biotechnology, vol. 33, pp. 73–80, 2015.

[11] J. D. Finn et al., "A single administration of CRISPR/Cas9 lipid nanoparticles achieves robust and persistent in vivo genome editing," Cell Reports, vol. 22, pp. 2227–2235, 2018.

[12] J. B. Miller et al., "Non-viral CRISPR/Cas gene editing in vitro and in vivo enabled by synthetic nanoparticle co-delivery of Cas9 mRNA and sgRNA," Angewandte Chemie International Edition, vol. 56, pp. 1059–1063, 2017.

[13] S. Wilhelm et al., "Analysis of nanoparticle delivery to tumours," Nature Reviews Materials, vol. 1, Art. no. 16014, 2016.

[14] N. Pardi et al., "mRNA vaccines—A new era in vaccinology," Nature Reviews Drug Discovery, vol. 17, pp. 261–279, 2018.

[15] X. Hou et al., "Lipid nanoparticles for mRNA delivery," Nature Reviews Materials, vol. 6, pp. 1078–1094, 2021.

[16] J. A. Kulkarni et al., "On the role of helper lipids in lipid nanoparticle formulations of siRNA," Nanoscale, vol. 11, pp. 21733–21746, 2019.

[17] M. Jayaraman et al., "Maximizing the potency of siRNA lipid nanoparticles for hepatic gene silencing in vivo," Angewandte Chemie International Edition, vol. 51, pp. 8529–8533, 2012.

[18] N. M. Belliveau et al., "Microfluidic synthesis of highly potent limit-size lipid nanoparticles for in vivo delivery of siRNA," Molecular Therapy – Nucleic Acids, vol. 1, Art. no. e37, 2012.

[19] J. S. Suk et al., "The penetration of large polymeric nanoparticles into fresh respiratory mucus," Proceedings of the National Academy of Sciences of the United States of America, vol. 106, pp. 654–659, 2009.

[20] Akinc et al., "The Onpattro story and the clinical translation of nanomedicines containing nucleic acid-based drugs," Nature Nanotechnology, vol. 14, pp. 1084–1087, 2019.

[21] D. Adams et al., "Patisiran, an RNAi therapeutic, for hereditary transthyretin amyloidosis," The New England Journal of Medicine, vol. 379, pp. 11–21, 2018.

[22] S. A. Dilliard et al., "On the mechanism of tissue-specific mRNA delivery by selective organ targeting nanoparticles," Proceedings of the National Academy of Sciences of the United States of America, vol. 118, Art. no. e2109256118, 2021.

[23] M. Qiu et al., "Lung-selective mRNA delivery of synthetic lipid nanoparticles for the treatment of pulmonary lymphangioleiomyomatosis," Proceedings of the National Academy of Sciences of the United States of America, vol. 119, Art. no. e2203356119, 2022.

[24] W. Gao et al., "Cargo-towing fuel-free magnetic nano swimmers for targeted drug delivery," Small, vol. 8, pp. 460–467, 2012.

[25] J. Li et al., "Enzyme-powered nanomotors: Emerging technologies for biomedical applications," Chemical Society Reviews, vol. 50, pp. 1957–1976, 2021.

[26] D. H. Kim et al., "Biofunctionalized magnetic-vortex microdiscs for targeted cancer-cell destruction," Nature Materials, vol. 9, pp. 165–171, 2010.

[27] Servant et al., "Magnetic microbots to fight cancer," Nanoscale, vol. 8, pp. 19914–19922, 2016.

[28] S. Martel et al., "MRI-based medical nanorobotic platform for the control of magnetic nanoparticles and flagellated bacteria for target interventions in human capillaries," The International Journal of Robotics Research, vol. 28, pp. 1169–1182, 2009.

[29] Y. Alapan et al., "Soft erythrocyte-based bacterial micro swimmers for cargo delivery," Science Robotics, vol. 3, Art. no. eaar4423, 2018.

[30] B. Wang et al., "Magnetically driven microrobots for biomedical applications," Advanced Materials, vol. 35, Art. no. 2207273, 2023.

[31] K. R. Kalli et al., "Folate receptor alpha as a tumor target in epithelial ovarian cancer," Gynecologic Oncology, vol. 108, pp. 619–626, 2008.

[32] D. J. O'Shannessy et al., "Folate receptor alpha expression in lung cancer: Diagnostic and prognostic significance," Oncotarget, vol. 8, pp. 93232–93252, 2017.

[33] K. N. Moore et al., "Folate receptor alpha as a target for ovarian cancer," Gynecologic Oncology Reports, vol. 39, Art. no. 100986, 2022.

[34] L. E. Kelemen, "The role of folate receptor alpha in cancer development, progression and treatment," Cancer and Metastasis Reviews, vol. 25, pp. 203–209, 2006.

[35] N. Parker et al., "Folate receptor expression in carcinomas and normal tissues determined by a quantitative radioligand binding assay," Analytical Biochemistry, vol. 338, pp. 284–293, 2005.

[36] P. S. Low and S. A. Kularatne, "Folate-targeted therapeutic and imaging agents for cancer,"

Current Opinion in Chemical Biology, vol. 13, pp. 256–262, 2009.

[37] S. Laurent et al., "Magnetic iron oxide nanoparticles: Synthesis, stabilization, vectorization, physicochemical characterizations, and biological applications," Chemical Reviews, vol. 108, pp. 2064–2110, 2008.

[38] O. S. Pak et al., "High-speed propulsion of flexible nanowire motors: Theory and experiments," Soft Matter, vol. 7, pp. 8169–8181, 2011.

[39] J. Heyes et al., "Synthesis and characterisation of novel ionisable lipids for siRNA delivery," Journal of Controlled Release, vol. 107, pp. 276–287, 2005.

[40] M. Jayaraman et al., "Conformational and positional stability of RNAi-triggering lipids in serum," Angewandte Chemie International Edition, vol. 51, pp. 12398–12403, 2012.

[41] F. Jiang et al., "Structures of Cas9 endonucleases reveal RNA-mediated conformational activation," Science, vol. 351, pp. 867–871, 2016.

[42] M. A. Moreno-Mateos et al., "CRISPRscan: Designing highly efficient sgRNAs for CRISPR-Cas9 targeting in vivo," Nature Methods, vol. 12, pp. 982–988, 2015.

[43] S. Bae et al., "Cas-OFFinder: A fast and versatile algorithm that searches for potential off-target sites of Cas9 RNA-guided endonucleases," Bioinformatics, vol. 30, pp. 1473–1475, 2014.

[44] G. M. Morris et al., "AutoDock4 and AutoDockTools4: Automated docking with selective receptor flexibility," Journal of Computational Chemistry, vol. 30, pp. 2785–2791, 2009.

[45] O. Trott and A. J. Olson, "AutoDock Vina: Improving the speed and accuracy of docking with a new scoring function, efficient optimization, and multithreading," Journal of Computational Chemistry, vol. 31, pp. 455–461, 2010.

[46] D. A. Case et al., AMBER 2022. San Francisco, CA, USA: University of California, 2022.

[47] S. Izadi et al., "ff15ipq-m: A protein force field with charge penetration and fluctuating multipoles," Journal of Physical Chemistry B, vol. 126, pp. 8511–8523, 2022.

[48] U. Essmann et al., "A smooth particle mesh Ewald method," Journal of Chemical Physics, vol. 103, pp. 8577–8593, 1995.

[49] D. R. Roe and T. E. Cheatham, "PTRAJ and CPPTRAJ: Software for processing and analysis of molecular dynamics trajectory data," Journal of Chemical Theory and Computation, vol. 9, pp. 3084–3095, 2013.

[50] S. C. Semple et al., "Rational design of cationic lipids for siRNA delivery," Nature Biotechnology, vol. 28, pp. 172–176, 2010.

[51] S. Willmann et al., "PK-Sim: A physiologically based pharmacokinetic whole-body model," Biosilico, vol. 1, pp. 121–124, 2003.

[52] L. Kuepfer et al., "Applied concepts in PBPK modeling: How to build a PBPK/PD model," CPT: Pharmacometrics & Systems Pharmacology, vol. 5, pp. 539–552, 2016.

[53] M. Li et al., "Physiologically based pharmacokinetic model of PEGylated liposomal doxorubicin in mice and rats," Journal of Pharmacokinetics and Pharmacodynamics, vol. 45, pp. 661–677, 2018.

[54] Nacev et al., "Towards reconstructing ancient grain boundaries through magnetic drug targeting," Physical Review Research, vol. 3, Art. no. 033213, 2021.

[55] M. Paulos et al., "Ligand binding and kinetics of folate receptor recycling in vivo: Impact on receptor-mediated drug delivery," Molecular Pharmacology, vol. 66, pp. 1406–1414, 2004.

[56] J. Yang et al., "Kinetic analysis of folate receptor recycling in vivo: Impact on receptor-mediated drug delivery," Journal of Controlled Release, vol. 172, pp. 266–273, 2013.

[57] J. P. Behr, "The proton sponge: A trick to enter cells the viruses did not exploit," Chimia, vol. 51, pp. 34–36, 1997.

[58] N. D. Sonawane et al., "Chloride accumulation and swelling in endosomes enhances DNA transfer by polyamine-DNA polyplexes," Journal of Biological Chemistry, vol. 278, pp. 44826–44831, 2003.

[59] J. A. Zuris et al., "Efficient cationic lipid-mediated delivery of CRISPR-Cas9 ribonucleoproteins for tissue-specific gene

editing," Nature Communications, vol. 11, Art. no. 2333, 2020.

[60] K. Lee et al., "Nanoparticle delivery of CRISPR into the brain rescues a mouse model of fragile X syndrome from exaggerated repetitive behaviours," Nature Biomedical Engineering, vol. 2, pp. 497–507, 2018.

[61] Ghosh and P. Fischer, "Controlled propulsion of artificial magnetic nanostructured propellers," Nano Letters, vol. 9, pp. 2243–2245, 2009.

[62] K. J. Hassett et al., "Optimization of lipid nanoparticles for intramuscular administration of mRNA vaccines," Molecular Therapy – Nucleic Acids, vol. 15, pp. 1–11, 2019.

[63] H. Nishimasu et al., "Crystal structure of Cas9 in complex with guide RNA and target DNA," Cell, vol. 156, pp. 935–949, 2014.

[64] C. Anders et al., "Structural basis of PAM-dependent target DNA recognition by the Cas9 endonuclease," Nature, vol. 513, pp. 569–573, 2014.

[65] F. Jiang et al., "CRISPR-Cas9 structures and mechanisms," Annual Review of Biophysics, vol. 46, pp. 505–529, 2017.

[66] S. H. Sternberg et al., "DNA interrogation by the CRISPR RNA-guided endonuclease Cas9," Nature, vol. 507, pp. 62–67, 2014.

[67] G. Palermo et al., "Understanding the mechanistic basis of non-coding RNA through molecular dynamics simulations," Journal of Structural Biology, vol. 206, pp. 267–279, 2019.

[68] S. Zheng and X. Huang, "Energy-based route to accelerate kinetic analysis of CRISPR-Cas9 cleavage," Journal of Chemical Theory and Computation, vol. 15, pp. 2876–2884, 2019.

[69] Y. S. Dagdas et al., "A conformational checkpoint between DNA binding and cleavage by CRISPR-Cas9," Science Advances, vol. 3, Art. no. eaao0027, 2017.

[70] J. S. Chen et al., "Enhanced proofreading governs CRISPR-Cas9 targeting accuracy," Nature, vol. 550, pp. 407–410, 2017.

[71] G. Palermo, "Structural and dynamic insights into the CRISPR-Cas9 system," Current Opinion in Structural Biology, vol. 62, pp. 225–233, 2020.

[72] G. Palermo et al., "Keys to CRISPR-Cas9 activity from the solution structure and dynamics of RNA-DNA heteroduplexes," Journal of the American Chemical Society, vol. 141, pp. 13061–13069, 2019.

[73] G. Palermo, "CRISPR-Cas9: The discovery, the biology, the therapeutic translation," Israel Journal of Chemistry, vol. 60, pp. 207–215, 2020.

[74] M. Shibata et al., "Real-space and real-time dynamics of CRISPR-Cas9 visualized by high-speed atomic force microscopy," Nature Communications, vol. 8, Art. no. 1430, 2017.

[75] M. Karimi et al., "pH-sensitive stimulus-responsive nanocarriers for targeted delivery of therapeutic agents," Wiley Interdisciplinary Reviews: Nanomedicine and Nanobiotechnology, vol. 8, pp. 696–716, 2016.

[76] W. Gao et al., "Inspired by mussel adhesion: Hydrophobicity-induced transitions of polydopamine for smart pH-responsive drug delivery," ACS Applied Materials & Interfaces, vol. 10, pp. 41035–41045, 2018.

[77] J. A. Kulkarni et al., "Design of lipid nanoparticles for in vitro and in vivo delivery of plasmid DNA," Nanomedicine, vol. 13, pp. 1667–1675, 2017.

[78] P. R. Cullis and M. J. Hope, "Lipid nanoparticle systems for enabling gene therapies," Molecular Therapy, vol. 25, pp. 1467–1475, 2017.

[79] K. Leung et al., "Lipid nanoparticle siRNA systems for silencing of the androgen receptor in human prostate cancer," Journal of Controlled Release, vol. 241, pp. 1–12, 2016.

[80] Y. Barenholz, "Doxil®—The first FDA-approved nano-drug: Lessons learned," Journal of Controlled Release, vol. 160, pp. 117–134, 2012.

[81] Gabizon et al., "Prolonged circulation time and enhanced accumulation in malignant exudates of doxorubicin encapsulated in polyethylene-glycol coated liposomes," Cancer Research, vol. 54, pp. 987–992, 1994.

[82] L. O. Mair et al., "Soft capsule magnetic millirobots for region-specific drug delivery in the central nervous system," Frontiers in Robotics and AI, vol. 8, Art. no. 702566, 2021.

[83] M. N. Albarghouthi et al., "Magnetic resonance navigation of gas-filled microrobots for image-guided drug delivery to ovarian cancer," Science Robotics, vol. 7, Art. no. eabm7316, 2022.

[84] S. Martel and M. Mohammadi, "Using a swarm of self-propelled natural microrobots in the form of flagellated bacteria to perform complex micro-assembly tasks," in Proc. IEEE Int. Conf. Robotics and Automation (ICRA), 2010, pp. 5005–5016.

[85] P. S. Low and A. C. Antony, "Folate receptor-targeted drugs for cancer and inflammatory diseases," Advanced Drug Delivery Reviews, vol. 56, pp. 1055–1058, 2004.

[86] W. Xia and P. S. Low, "Folate-targeted therapies for cancer," Journal of Medicinal Chemistry, vol. 53, pp. 6811–6824, 2010.

[87] R. Hilgenbrink and P. S. Low, "Folate receptor-mediated drug targeting: From therapeutics to diagnostics," Journal of Pharmaceutical Sciences, vol. 94, pp. 2135–2146, 2005.

[88] R. V. Benjaminsen et al., "The possible 'proton sponge' effect of polyethylenimine (PEI) does not include change in lysosomal pH," Molecular Therapy, vol. 18, pp. 164–171, 2013.

[89] Akinc et al., "A combinatorial library of lipid-like materials for delivery of RNAi therapeutics," Nature Biotechnology, vol. 26, pp. 561–569, 2008.

[90] H. X. Wang et al., "CRISPR/Cas9-based genome editing for disease modeling and therapy," Cellular and Molecular Life Sciences, vol. 73, pp. 4303–4317, 2016.

[91] C. A. Lino et al., "Delivering CRISPR: A review of the challenges and approaches," Drug Delivery, vol. 25, pp. 1234–1257, 2018.

[92] M. H. Porteus, "A new class of medicines through DNA editing," New England Journal of Medicine, vol. 380, pp. 947–959, 2019.

[93] M. A. Oberli et al., "Lipid nanoparticle assisted mRNA delivery for potent cancer immunotherapy," Nano Letters, vol. 17, pp. 1326–1335, 2017.

[94] J. C. Kaczmarek et al., "Advances in the delivery of RNA therapeutics: From concept to clinical reality," Genome Medicine, vol. 9, Art. no. 60, 2017.

[95] European Medicines Agency, ICH Topic S6: Preclinical Safety Evaluation of Biotechnology-Derived Pharmaceuticals, EMA/CHMP/ICH/731268/1998, 2011.

[96] G. T. Kozma et al., "Pseudo-anaphylaxis to polyethylene glycol (PEG)-coated liposomes: Roles of anti-PEG IgM and complement activation in a porcine model of human infusion reactions," ACS Nano, vol. 14, pp. 9785–9799, 2020.

[97] M. S. Kormann et al., "Expression of therapeutic proteins after delivery of chemically modified mRNA in mice," Nature Biotechnology, vol. 29, pp. 154–157, 2011.

[98] N. Pardi et al., "Expression kinetics of nucleoside-modified mRNA delivered in lipid nanoparticles to mice by various routes," Journal of Controlled Release, vol. 217, pp. 345–351, 2015.

[99] W. Gao and J. Wang, "Synthetic micro/nanomotors in drug delivery," Nanoscale, vol. 6, pp. 10486–10494, 2014.

[100] S. Campuzano et al., "Nanomotors in sensing and biosensing," Sensors and Actuators B: Chemical, vol. 240, pp. 738–753, 2017.

[101] L. Zhang et al., "Templated assembly of magnetic nanoparticles via controlled magnetic dipole–dipole attraction for imagable and actuatable microcapsule motors," Journal of Materials Chemistry A, vol. 3, pp. 8640–8649, 2015.

[102] H. Xu et al., "Sperm-hybrid micromotor for targeted drug delivery," ACS Nano, vol. 12, pp. 327–337, 2018.

[103] K. Gupta and M. Gupta, "Synthesis and surface engineering of iron oxide nanoparticles for biomedical applications," Biomaterials, vol. 26, pp. 3995–4021, 2005.

[104] S. Kim et al., "CRISPR RNAs guide immunity in Streptococcus pyogenes," mBio, vol. 7, Art. no. e00451-16, 2016.

[105] S. Ling et al., "Lentiviral delivery of co-packaged Cas9 mRNA and a Vegfa-targeting guide RNA prevents wet age-related macular degeneration in mice," Nature Biomedical Engineering, vol. 5, pp. 144–156, 2021.

[106] Hendel et al., "Chemically modified guide RNAs enhance CRISPR-Cas genome editing in

human primary cells," Nature Biotechnology, vol. 33, pp. 985–989, 2015.

[107] S. H. Sternberg et al., "Conformational control of DNA target cleavage by CRISPR-Cas9," Nature, vol. 527, pp. 110–113, 2015.

[108] B. D. Slaughter et al., "Origins and consequences of nuclear envelope proteins in the endoplasmic reticulum," Developmental Cell, vol. 29, pp. 137–144, 2014.

[109] D. J. O'Shannessy et al., "Folate receptor alpha expression in ovarian cancer: Association with the clear cell and mucinous histological subtype and the outcome of treatment with pegylated liposomal doxorubicin," Journal of Experimental & Clinical Cancer Research, vol. 31, Art. no. 63, 2012.

[110] S. N. Tchaikovski and J. W. Olver, "Folate receptor-mediated targeting and intracellular delivery of therapeutic and imaging agents," Pharmaceutics, vol. 13, Art. no. 2185, 2021.

[111] U. A. Matulonis et al., "Efficacy and safety of mirvetuximab soravtansine in patients with platinum-resistant ovarian cancer with high folate receptor alpha expression," Journal of Clinical Oncology, vol. 39, pp. 2432–2441, 2021.

[112] Y. V. Kovtun et al., "A CD30-specific MMAE antibody-drug conjugate exhibits potent antitumor activity and improved tolerability in preclinical models," Cancer Research, vol. 75, p. 857, 2015.

[113] K. Varkouhi et al., "Endosomal escape pathways for delivery of biologicals," Journal of Controlled Release, vol. 151, pp. 220–228, 2011.

[114] Wittrup et al., "Visualizing lipid-formulated siRNA release from endosomes and target gene knockdown," Nature Biotechnology, vol. 33, pp. 870–876, 2015.

[115] J. A. Kulkarni et al., "On the formation and morphology of lipid nanoparticles containing ionizable cationic lipids and siRNA," ACS Nano, vol. 12, pp. 4787–4795, 2018.

[116] K. Leung et al., "Lipid nanoparticles containing siRNA synthesized by microfluidic mixing exhibit an electron-dense nanostructured core," Journal of Physical Chemistry C, vol. 116, pp. 18440–18450, 2012.

[117] D. Wang et al., "Adeno-associated virus vector as a platform for gene therapy delivery," Nature Reviews Drug Discovery, vol. 18, pp. 358–378, 2019.

[118] P. R. Cullis and M. T. Litzinger, "Drug delivery systems: Entering the mainstream," Science, vol. 373, p. 1472, 2021.

[119] S. J. Marrink et al., "Computational modeling of realistic cell membranes," Chemical Reviews, vol. 119, pp. 6184–6226, 2019.

[120] T. Stylianopoulos et al., "Causes, consequences, and remedies for growth-induced solid stress in murine and human tumors," Proceedings of the National Academy of Sciences of the USA, vol. 109, pp. 15101–15108, 2012.

[121] R. J. Ihry et al., "p53 inhibits CRISPR-Cas9 engineering in human pluripotent stem cells," Nature Medicine, vol. 24, pp. 939–946, 2018.

[122] E. Haapaniemi et al., "CRISPR-Cas9 genome editing induces a p53-mediated DNA damage response," Nature Medicine, vol. 24, pp. 927–930, 2018.